PROCEEDINGS OF SPIE

SPIEDigitalLibrary.org/conference-proceedings-of-spie

3-D SAR imaging for multistatic GPR

Pereira, Mauricio, Zhang, Yu, Huston, Dryver, Xia, Tian

Mauricio Pereira, Yu Zhang, Dryver Huston, Tian Xia, "3-D SAR imaging for multistatic GPR," Proc. SPIE 10980, Image Sensing Technologies: Materials, Devices, Systems, and Applications VI, 109801D (13 May 2019); doi: 10.1117/12.2519430



Event: SPIE Defense + Commercial Sensing, 2019, Baltimore, Maryland, United States

3-D SAR Imaging for Multistatic GPR

Mauricio Pereira, Yu Zhang, Dryver Huston, and Tian Xia

University of Vermont, School of Engineering, Burlington, VT 05405, USA.

ABSTRACT

Ground penetrating radar (GPR) is a remote geophysical sensing method that has been applied in the localization of underground utilities, bridge deck survey, localization of landmines, mapping of terrain for aid in driverless cars, etc. Multistatic GPR can deliver a faster survey, wider spatial coverage, and multiple viewpoints of the subsurface. However, because of the transmit and receive antennas spatial offset, formation of 3D GPR image by simple stacking of the acquired A-scans is inaccurate. Also, averaging of different receivers data may lead to destructive interference of back-scattered waves due to different time delays implied by the spatial offset, so averaging does not lead to higher SNR in general. Furthermore, the energy back-scattered by scatter points are spread in hyperbolas in the GPR raw data. Migration or imaging algorithms are employed to increase SNR by focusing the hyperbolas. This focusing process also leads to better accuracy in target localization. In this paper, a computationally efficient synthetic aperture radar (SAR) imaging algorithm that properly integrates multistatic GPR data in both ground and air-coupled cases is presented. The algorithm is successfully applied on two synthetic datasets.

Keywords: Synthetic Aperture Radar, Ground Penetrating Radar, Multistatic Radar, 3-D Imaging

1. INTRODUCTION

Ground penetrating radar (GPR) is a remote geophysical sensing method based on the scattering of electromagnetic waves emitted into the ground.^{1–3} It has applications in the localization of underground infrastructure,⁴ assessment of bridge decks,^{5,6} landmine and buried unexploded ordnance detection,^{7–9} rebar detection,^{10–13} pipe leakage detection,¹⁴ railroad inspection,¹⁵ self-driving cars,¹⁶ etc.

Multistatic GPR can decrease survey time, with direct application, for instance, in the assessment of bridge deck structural health. In multistatic radar systems the spatial offset of the transmit and receive antennas will imply different scattered signal delays, such that simple stacking of collected datasets do not yield a faithful 3D image of the subsurface. This poses a problem on how to appropriately account for the antennas spatial offset when fusing each transmitter-receiver dataset.

Furthermore, scatter points appear as hyperbolas in GPR data. These hyperbolas may be focused to improve SNR through migration or imaging algorithms, facilitating data interpretation and improving accuracy in target localization.¹ The focusing of the back-scattered wave is an inverse problem that stems from Maxwell's equation of electromagnetism.^{17,18} There are techniques that may resolve the inverse problem using the Born approximation, ^{15,19} but they are computationally intensive. Alternative imaging algorithms avoid the inverse problem altogether by exploiting the direct calculation of time or phase delays. For instance, the back-projection algorithm is a time-domain migration algorithm based on projecting the back-scattered waves into the spatial domain using the wave two-way travel time.^{20,21} This method is prone to parallelization and suitable for layered media, but it is both computation and memory intensive. Frequency-based imaging algorithms, sometimes considered to form a class under Fourier imaging methods,²² can be highly efficient if stated in a form suitable for Fast Fourier Transforms (FFTs) and achieve image formation faster than the BPA without relying on GPU-powered parallel processing.

Synthetic aperture radar (SAR) imaging may be implemented using Fourier transforms.^{23,24} The SAR algorithm is widely applied in the formation of satellite imagery as it improves resolution by synthetically increasing the antenna aperture. However, most of the literature regarding SAR imaging considers single layered media (either air or ground) and/or monostatic radar.^{25–30} For through-the-wall radar (TWR) Fourier imaging methods, some algorithms that include the delay caused by the wall, and multistatic radar systems, have been

Image Sensing Technologies: Materials, Devices, Systems, and Applications VI, edited by Nibir K. Dhar, Achyut K. Dutta, Sachidananda R. Babu, Proc. of SPIE Vol. 10980, 109801D · © 2019 SPIE CCC code: 0277-786X/19/\$18 · doi: 10.1117/12.2519430

proposed but they rely on the assumption of a plane wavefront.³¹ That is not a valid assumption, for instance, in landmine detection.

Here, a SAR imaging algorithm for both ground and air-coupled multistatic GPR is presented. The method uses a synthetically generated reference image to estimate the phase function using FFTs for both ground and air-coupled multistatic GPR without assuming plane wavefront, and that is less computationally intensive than the BPA. Furthermore, the approach avoids the solution of a nonlinear system of equations that emerge in the development of bistatic SAR imaging.

This paper is organized as follows: In section 2, the generic SAR imaging algorithm is formulated. In section 2.1, the formulation is specialized for monostatic GPR. In sections 2.2 and 2.3, the bistatic SAR formulation and the proposed method are presented. In section 2.4, the method is extended to multistatic GPR. In section 3, an outline of the algorithm is presented, and the results of the algorithm applied to two synthetic datasets are presented and discussed. In section 4, a summary of the method is given, as well as a discussion of potential future research and applications.

2. SYNTHETIC APERTURE RADAR IMAGING

In SAR imaging, a relation between the desired subsurface image and the GPR data is established in the frequency domain. This relation enables the determination of the processing steps required to recover the image from the acquired GPR data.

Considering a real-valued, frequency independent reflectivity σ_i for i = 1...N discrete points in the subsurface domain of interest, the subsurface image may be expressed as

$$I(\mathbf{r}) = \sum_{i}^{N} \sigma_{i} \delta(\mathbf{r} - \mathbf{r}_{i}), \tag{1}$$

where $\mathbf{r} = [x, y, z]^T$ is the position of interest, $\mathbf{r}_i = [x_i, y_i, z_i]^T$ is the position of the i^{th} discrete point, and $\delta(\bullet)$ is the Kroenecker delta.

The SAR imaging algorithm is employed to determine the unknown reflectivities σ_i 's in a qualitative sense, i.e., the interest is in determining the contrast of the image and not recovering the actual physical value of the subsurface reflectivity.

The Fourier transform in space of (1) is

$$\mathcal{I}(\mathbf{k_r}) = \sum_{i}^{N} \sigma_i exp(-j\mathbf{k_r} \cdot \mathbf{r_i}), \tag{2}$$

where $\mathbf{k_r} = [k_x, k_y, k_z]^T$ are the corresponding wavenumbers of $\mathbf{r} = [x, y, z]^T$. Notice that the phase function is linear in space.

In a traditional GPR survey, a received signal, also known as A-scan, is recorded at each system location in a regular grid. A-scans may be stacked as a 2D matrix to compose a B-scan, or as a 3D matrix to compose a C-scan. The acquired 3D GPR data is referred as a C-scan henceforth, and modeled as

$$s(x', y', t) = \sum_{i}^{N} \sigma_{i} p(t - \tau_{i}(\mathbf{r}_{i}, x', y')), \tag{3}$$

where p(t) is the emitted signal, $\tau_i(\mathbf{r_i}, x', y')$ is the signal delay whose explicit function form depends on the GPR type (e.g. monostatic or multistatic) and coupling (e.g. air or ground-coupled).

The Fourier transform in time of (3) is

$$S(x', y', \omega) = P(\omega) \sum_{i}^{N} \sigma_{i} exp(-j\omega \tau_{i}(\mathbf{r}_{i}, x', y'))), \tag{4}$$

and following with the Fourier transform in space yields

$$S(k_x', k_y', \omega) = P(\omega) \sum_{i}^{N} \sigma_i \mathcal{F}_{x'y'} \{ exp(-j\omega \tau_i(\mathbf{r_i}, x', y')) \},$$
 (5)

where k'_x and k'_y are the wavenumbers corresponding to x' and y', respectively, and $P(\omega) = \mathcal{F}_t\{p(t)\}$ is the time Fourier transform of the GPR emitted signal.

In the SAR imaging algorithm presented here, a suitable relation between the Fourier-transformed GPR data $S(k'_x, k'_y, \omega)$ and the Fourier-transformed domain image $\mathcal{I}(\mathbf{k_r})$ must be determined so that computationally efficient inverse FFTs can be used to recover the subsurface image $I(\mathbf{r})$.

In the developments below, each layered media is considered homogeneous.

2.1 Monostatic ground-coupled GPR

For monostatic, ground-coupled GPR (see Fig. 1) the signal delay is given by

$$\tau_i(\mathbf{r_i}, x', y') = \frac{2}{v} \|\mathbf{r_{TR}}(x', y') - \mathbf{r_i}\|,\tag{6}$$

where $v = c/\sqrt{\epsilon}$ is the wave speed, c is the speed of light, ϵ is the ground dielectric constant, $\mathbf{r_{TR}}$ is the transceiver position, and \mathbf{r}_i is the i^{th} domain point position and $\| \bullet \|$ is the l_2 -norm.

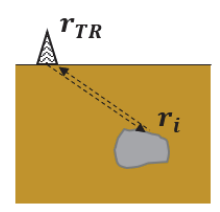


Figure 1. Diagram of a monostatic ground-coupled ground penetrating radar imaging setup.

For a delay of form (6), equation (5) becomes²³

$$S(\mathbf{k_r}') = P(\omega) \sum_{i}^{N} \sigma_i exp(-j\mathbf{k_r}' \cdot \mathbf{r_i}), \tag{7}$$

where $\mathbf{k_r}' = [k_x', k_y', k_z']^T$, $k_z' = \sqrt{4k^2 - k_x'^2 - k_y'^2}$, and $k = \omega/v$.

Notice that the phase function is linear in space as is (2). Thus, when $\mathbf{k'_r} = \mathbf{k_r}$,

$$S(\mathbf{k_r}) = P(\omega) \sum_{i}^{N} \sigma_i exp(-j\mathbf{k_r} \cdot \mathbf{r_i}) = P(\omega) \mathcal{I}(\mathbf{k_r}).$$
(8)

The image is approximately recovered by taking the inverse Fourier transform

$$I(\mathbf{r}) \approx \mathcal{F}_{xyz}^{-1}\{|P(\omega)|^2 \mathcal{I}(\mathbf{k_r})\} = \mathcal{F}_{xyz}^{-1}\{P^*(\omega)\mathcal{S}(\mathbf{k_r})\}. \tag{9}$$

If interpolation in frequency domain is not performed before computing the inverse transform above, the resulting third coordinate is in time unit and a mapping between time and space is required to determine the correct depth. Here, an approximation that the antenna has a small beamwidth is used such that cross-range compression and pulse compression can be performed independently. Then, a simplified mapping between time

and depth may be used, analogous to the use of the Fresnel approximation.²³ In this case, the mapping is given by

$$z = \frac{vt}{2}. (10)$$

2.2 Bistatic ground-coupled GPR

For the bistatic, ground-coupled GPR (see Fig. 2) the phase delay is given by

$$\tau_i(\mathbf{r_i}, x', y') = \frac{\|\mathbf{r_T}(x', y') - \mathbf{r_i}\| + \|\mathbf{r_R}(x', y') - \mathbf{r_i}\|}{v}.$$
(11)

The transmitter and receiver that compose the GPR system move together, such that the transmitter position $\mathbf{r_T}$ and receiver position $\mathbf{r_R}$ are given in terms of (x', y').

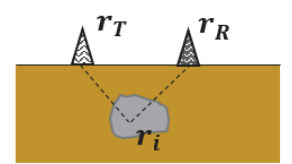


Figure 2. Diagram of a bistatic ground-coupled ground penetrating radar imaging setup.

In this case, extending Soumekh's³² approach to 3D, the transform (5) can be represented as

$$S(k_x', k_y', \omega) = P(\omega) \sum_{i=1}^{N} \sigma_i \int \int exp(-j\Psi(\mathbf{k}_r', \alpha_x, \alpha_y)) d\alpha_x d\alpha_y, \tag{12}$$

where $\Psi(\mathbf{k}'_{\mathbf{r}}, \alpha_x, \alpha_y)$ is a phase function, α_x , α_y are dummy variables analogous to wavenumbers. As will be discussed ahead, the explicit form of $\Psi(\mathbf{k}'_{\mathbf{r}}, \alpha_x, \alpha_y)$ is not relevant in the approach presented here. Using the stationary phase method (SPM),^{23,33} where the leading order term of the Taylor series about a stationary point dominates the integral value, leads to

$$S(\mathbf{k}_{\mathbf{r}}') = P(\omega) \sum_{i}^{N} \sigma_{i} exp(-j\hat{\Psi}(\mathbf{k}_{\mathbf{r}}')), \tag{13}$$

where $\hat{\Psi}(\mathbf{k'_r}) = \Psi(\mathbf{k'_r}, \hat{\alpha}_x, \hat{\alpha}_y)$ is the phase function evaluated at the stationary point and the starred variables $\hat{\alpha}_u$, $\hat{\alpha}_v$ correspond to the stationary point, satisfying

$$\nabla \Psi(\mathbf{k}_{\mathbf{r}}', \hat{\alpha}_u, \hat{\alpha}_v) = \mathbf{0},\tag{14}$$

where $\nabla = [\partial(\bullet)/\partial\alpha_u, \partial(\bullet)/\partial\alpha_v]^T$.

The system (14) is nonlinear and a closed form solution is not straightforward.³² Furthermore, even if a closed form solution is found, it is not clear that the resulting phase function would be linear in space, thus not prone to direct application of standard FFT.

Soumekh³² suggests that $\hat{\Psi}(\mathbf{k'_r}) = \Psi(\mathbf{k'_r}, \hat{\alpha}_x, \hat{\alpha}_y)$ be approximated as

$$\hat{\Psi}(\mathbf{k}_{\mathbf{r}}') \approx \Psi_0 + \mathbf{k}_{\mathbf{r}} \cdot \mathbf{r}_{\mathbf{i}},\tag{15}$$

where the phase term Ψ_0 absorbs nonlinearities, for instance, due to offset between transmit and receive antennas or due to change of media velocities.

Introducing (15) in (13), the transformed signal becomes

$$S(\mathbf{k_r}) = P(\omega)exp(-j\Psi_0)\sum_{i}^{N} \sigma_i exp(-j\mathbf{k_r} \cdot \mathbf{r_i}) = P(\omega)exp(-j\Psi_0)\mathcal{I}(\mathbf{k_r}), \tag{16}$$

and the image is recovered as

$$I(\mathbf{r}) \approx \mathcal{F}_{xuz}^{-1} \{ P^*(\omega) exp(j\Psi_0) \mathcal{S}(\mathbf{k_r}) \}.$$
 (17)

Determining Ψ_0 requires numerically solving the nonlinear system (14) for each system position and domain point. But Ψ_0 does not depend on the reflectivity of the domain points, and it is reasonable to expect that it is strongly dependent on the GPR system arrangement and domain discretization, as τ_i (see Eq. (11)) explicitly depends on both.

Hence, if an image $\mathcal{I}_{ref}(\mathbf{r})$, transmitted signal spectrum $P_{ref}(\omega)$, and C-scan Fourier-transform $\mathcal{S}_{ref}(\mathbf{k_r})$, are given under the same GPR system arrangement and domain of interest, equation (16) can be solved for the phase Ψ_0 instead. Notice that the signal $s_{ref}(x', y', t)$ may be generated using a simplified delay-only simulation that is fast to compute. Another possibility is to generate the reference signal by performing a calibration scan in the environment of interest.

Thus, the phase term $exp(-j\Psi_0)$ may be determined as

$$exp(-j\Psi_0) = P_{ref}^*(\omega)\mathcal{I}_{ref}^*(\mathbf{k_r})\mathcal{S}_{ref}(\mathbf{k_r})$$
(18)

where the amplitude terms were omitted.

Once the phase Ψ_0 is known, expression (17) is used to calculate the reflectivity of any C-scan collected using the same GPR arrangement and subsurface domain resolution.

2.3 Bistatic air-coupled GPR

In the bistatic, air-coupled GPR, assuming a flat ground surface (see Fig. 4), the delay is given by

$$\tau_{i} = \frac{\|\mathbf{r}_{\mathbf{T}}(x', y') - \mathbf{r}_{\mathbf{S}_{\mathbf{T}}}(\mathbf{r}_{i}, x', y')\|}{c} + \frac{\|\mathbf{r}_{\mathbf{S}_{\mathbf{T}}}(\mathbf{r}_{i}, x', y') - \mathbf{r}_{i}\|}{v} + \frac{\|\mathbf{r}_{i} - \mathbf{r}_{\mathbf{S}_{\mathbf{R}}}(\mathbf{r}_{i}, x', y')\|}{v} + \frac{\|\mathbf{r}_{\mathbf{S}_{\mathbf{R}}}(\mathbf{r}_{i}, x', y') - \mathbf{r}_{\mathbf{R}}(x', y')\|}{c}, \quad (19)$$

where $\mathbf{r_{S_T}}$ and $\mathbf{r_{S_R}}$ are the ground scattering points associated with the transmitter and receiver, respectively.

In the derivation of equation (12), not shown here, the SPM is also employed, which requires the calculation of the gradient of the phase function and solution of the resulting system of equations.³³

In the air-coupled scenario, the scattering points position depends both on the antennas position and the domain point of interest. To exactly determine the scattering points $\mathbf{r_{S_T}}$ and $\mathbf{r_{S_R}}$ as a function of x', y' and $\mathbf{r_i}$, using Snell's law, involves solving a fourth order polynomial equation.²¹ After solving for the scattering points, it would still be necessary to calculate the gradient of the resulting phase function to find the stationary point. Hence, the determination of the stationary phase is not straightforward. Also, even if the expression was determined, the SPM will need to be applied again to solve the double integral in an expression of the same form of (12), which entails solving a non-trivial nonlinear system of equations (Notice that this can be inferred based on the fact that the ground-coupled bistatic case, that leads to a nonlinear system of equations, is a particular case of equation (19) when $\epsilon = 1$ or c is set to v in (11)), and may result in a phase that is nonlinear in space. That is not desirable if efficient computation using FFT is preferred.

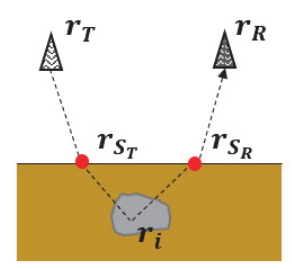


Figure 3. Diagram of a bistatic air-coupled ground penetrating radar imaging setup.

Instead, suppose that the bistatic air-coupled signal may be related to the image of interest in an equation of the same form of expression (16). Then a reference image and reference signal that considers both the air and ground layers is used to solve for the phase Ψ_0 via equation (18).

As in the monostatic case, the recovered image depth axis will be in time unit, so an appropriate mapping must be employed for the correct positioning of buried targets. However, in this case, there is not an explicit expression, since the exact calculation of the scattering point was avoided and the transmitter and receiver are spatially offset. To address that issue, a subsurface depth of interest is predetermined and discretized. The receiver is used as reference and is positioned above the discretized points, as illustrated in Fig. 2.3. Then, a mapping between travel time and depth is calculated for the air-coupled case using the same approach applied to generate the reference synthetic C-scan (for an example, see Fig. 5). In the implementation used to generate the results presented in section 3, an approximation of the scattering point position²⁰ was used to generate the reference synthetic C-scan.

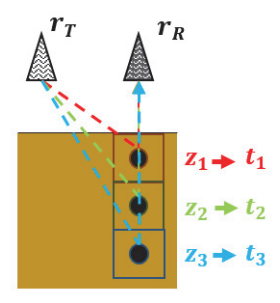


Figure 4. Diagram of depth-time mapping setup.

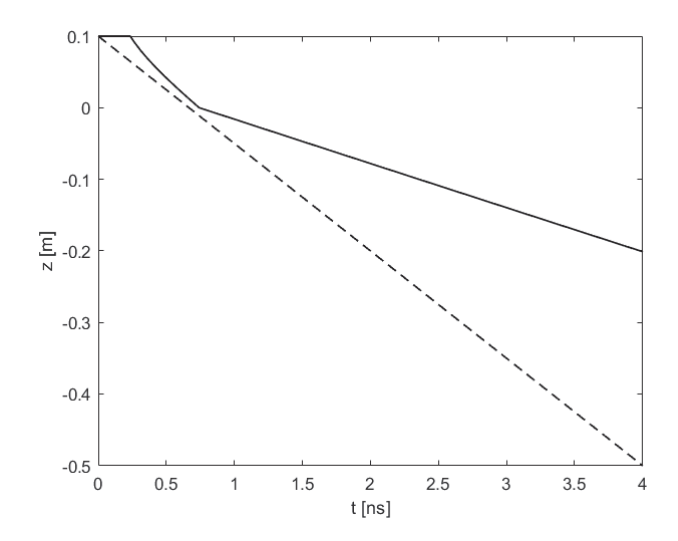


Figure 5. Scaling between depth and time axis for the first receiver. The dashed line represents the position given by assuming a constant speed c, the solid line represents the position considering the change in wave speed and antennas offset.

2.4 Multistatic GPR

Consider a multistatic GPR system with L transmitters and M receivers. Each transmit antenna sends a signal at a time such that the l^{th} transmitter and m^{th} receiver C-scan $s_{lm}(x', y', t)$ may be treated as a bistatic C-scan. Then the image of the l^{th} transmitter and m^{th} receiver $I_{lm}(x)$ is calculated following section 2.2 or 2.3 for ground or air-coupled, respectively.

The images for distinct transmitter and receiver pair of the multistatic GPR can not be simply added since the images are not located at the same spatial coordinates.

For the global image $\mathcal{G}(\mathbf{r})$, a region of interest \mathcal{D} is defined and discretized. Each transmitter-receiver pair image I_{lm} , l = 1...L, m = 1...M, is added to $\mathcal{G}(\mathbf{r})$ by linear interpolation.

The image $\mathcal{G}(\mathbf{r})$ is initialized as a zero 3D matrix. A simple heuristic is introduced to mitigate overestimation of the reflectivity strength of over-illuminated areas: If the current entry is null, simply insert the new value, otherwise average the current and new entry value. Another approach is to average each voxel by the number of observations (e.g. if a voxel received contributions from N datasets, divide the value by N), however this requires tracking of the number of observations. The multistatic SAR imaging algorithm is summarized below in algorithm 1, where it is assumed that $P_{ref}(\omega) = P(\omega)$. Although not explicitly stated, each transmitter-receiver pair image may be calculated in parallel for faster computation.

3. RESULTS

To qualitatively evaluate the imaging performance of the method described in section 2.4, the algorithm was applied to two synthetic air-coupled datasets. In both cases, the antennas setup, illustrated in Fig. 6, consists of a single transmitter, initially positioned at $\mathbf{r_T} = [0.05, 0.1, 0.1]^T$ (m), and three receivers initially positioned at $\mathbf{r_{R1}} = [0.05, 0.05, 0.1]^T$ (m), $\mathbf{r_{R2}} = [0.05, 0.1, 0.1]^T$ (m), and $\mathbf{r_{R3}} = [0.05, 0.15, 0.1]^T$ (m). The system generates a B-scan by moving 25 steps of $\Delta x = 0.01$ m. A total of 9 B-scans are collected each apart by $\Delta y = 0.02$ m. The emitted signal is a Ricker wave of 2 GHz. Each waveform consists of 1040 points over a window of 4 ns.

In the first case, the C-scan of a single point target is generated using a delay calculation, i.e., changes in the returning wave shape and amplitude are not considered, only the wave two-way travel time. As mentioned before, the determination of the exact position of the ground scattering point is computationally intensive. Instead, an approximation²⁰ is used, where the scattering point is given by two cases depending on the distance between the transmitter or receiver and the point of interest so that the fourth order polynomial does not need to be solved.

Algorithm 1 Multistatic SAR imaging algorithm

```
1: \mathcal{G}(x, y, z) = zeros(N_x, N_y, N_z)
 2: Define global domain axis vectors x_D, y_D, z_D.
 3: P(\omega) = FFT(p(t))
 4: for l = 1...L do
         for m = 1...M do
 5:
              Generate reference I_{ref}(\mathbf{r}) in local coordinates
 6:
             \mathcal{I}_{ref}(\mathbf{k_r}) = FFT(I_{ref}((r)))
 7:
             Generate s_{ref}(x', y', t)
                                                                                                                    ▷ Compute delays only.
 8:
             S_{ref} = FFT(s_{ref}(x', y', t))
 9:
             exp(-j\Psi_0) = P^*(\omega)\mathcal{I}_{ref}^*(\mathbf{k_r})\mathcal{S}_{ref}(x',y',t)
10:
              S_{lm}(\mathbf{k}_r) = FFT(s_{lm}(x', y', t))
11:
              I_{lm}(\mathbf{r}) = IFFT(exp(j\Psi_0)P^*(\omega)\mathcal{S}_{lm}(\mathbf{k_r}))
12:
13:
              for i = 1...N_x do
                                                                                                                     ▶ Add to global image
                  for j = 1...N_u do
14:
                       for k = 1...N_z do
15:
                                                                             \triangleright The z = f(t) mapping is used in the interpolation.
                           if G(i, j, k) == 0 then
16:
                                \mathcal{G}(i,j,k) = I_{lm}(x_D(i), y_D(j), z_D(k))
17:
18:
                               \mathcal{G}(i,j,k) = \frac{\mathcal{G}(i,j,k) + I_{lm}(x_D(i),y_D(j),z_D(k))}{2}
19:
20:
                       end for
21:
                  end for
22:
23:
              end for
24:
         end for
25: end for
```

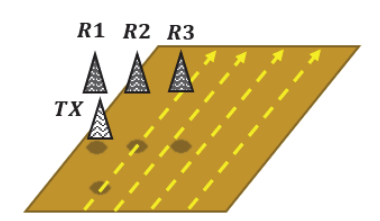


Figure 6. Diagram of the multistatic antenna setup used in the gprMax simulations.

The second case uses gprMax,³⁴ a finite-difference time-domain physics-based GPR simulator, to generate the C-scan of a metal plate. An ideal Hertzian dipole is used as the transmit antenna. The plate is a square of side 0.1 m and thickness 0.02 m and it is positioned at the center of the domain buried at a depth of 0.1 m. To generate the reference signal, used in the calculation of the Ψ_0 term, the same simplified delay calculation used in the first case is applied.

In both cases the domain $\mathcal{D} = [0.1, 0.3] \times [0.1, 0.3], [0, -0.2]$ (m^3) is discretized in $N_x \times N_y \times N_z = 40 \times 40 \times 50 = 80,000$ points.

3.1 Unity point scatterer

Figures 7 through 9 show both the synthetic C-scan and the resulting SAR image for each transmitter-receiver pair. Notice that the range of the x-y coordinates changes for each transmitter-receiver pair, but the point is shifted accordingly, matching the real location. The final multistatic image is shown in Fig. 10. The scattering point is correctly positioned in the 3D space.

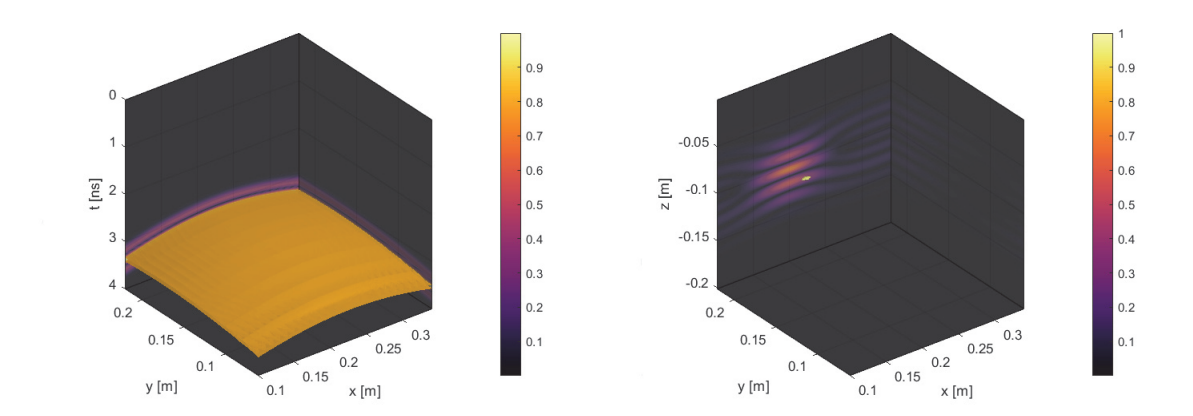


Figure 7. Unity scatter point S11 C-scan (left) and resulting 3D SAR image (right) isosurfaces at a value v = 0.9.

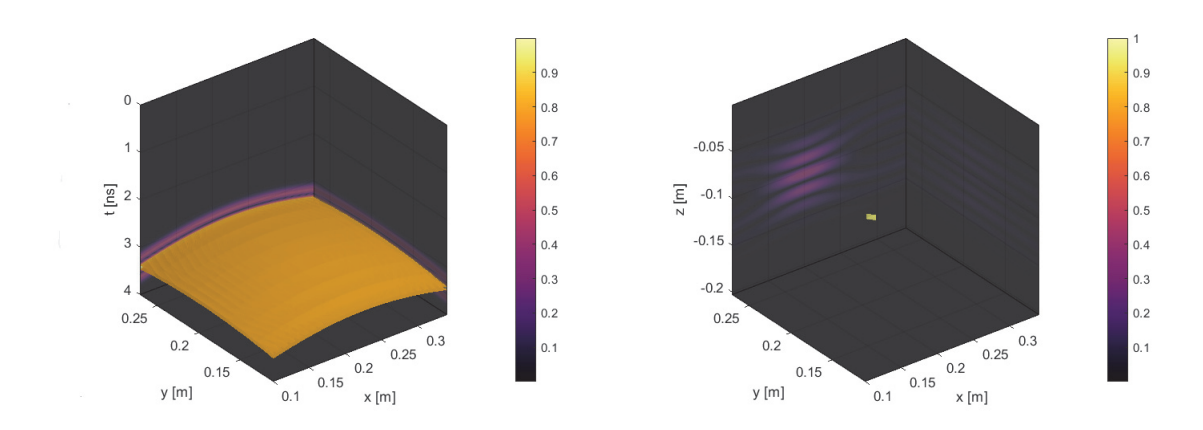


Figure 8. Unity scatter point S12 C-scan (left) and resulting 3D SAR image (right) isosurfaces at a value v = 0.9.

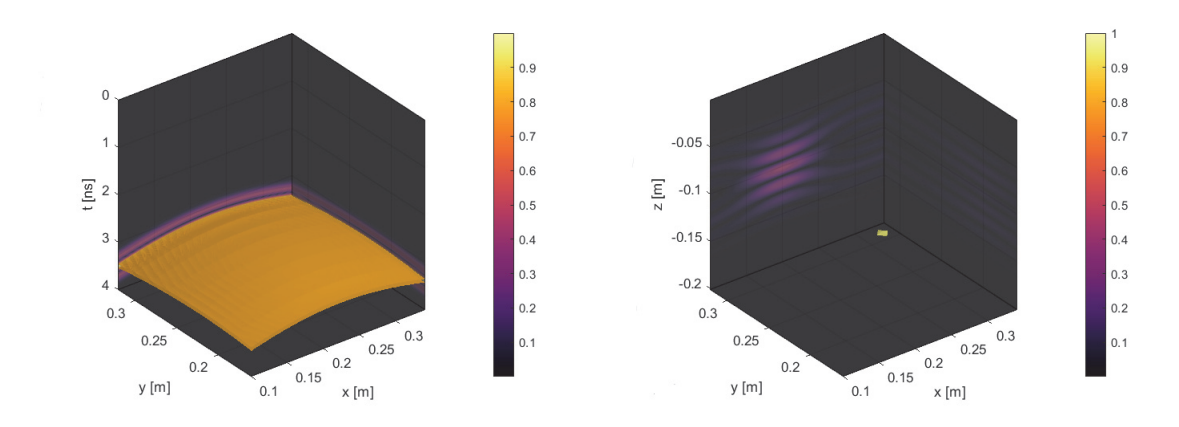


Figure 9. Unity scatter point S13 C-scan (left) and resulting 3D SAR image (right) isosurfaces at a value v = 0.9.

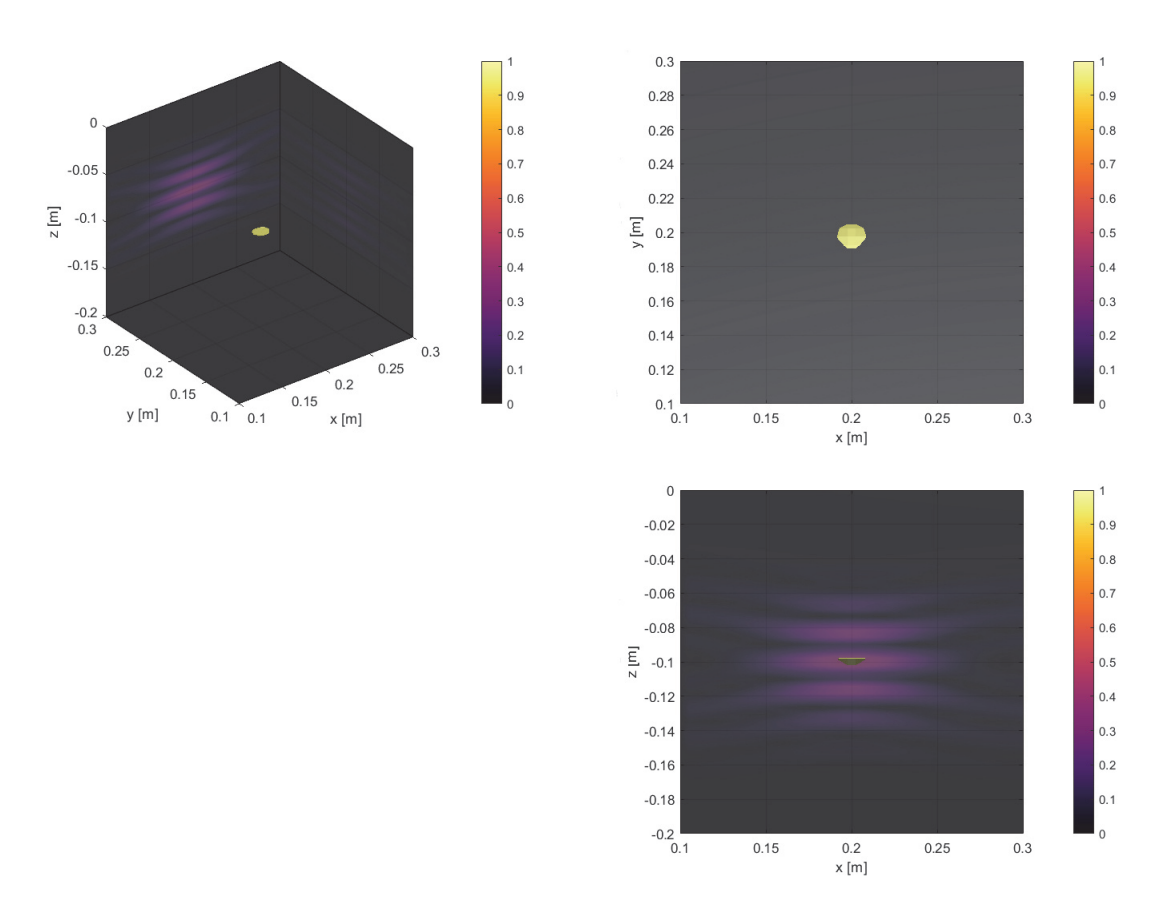


Figure 10. Final unity scatter point 3D multistatic image isosurface at v = 0.9.

3.2 Plate

Figures 11 through 13 show both the synthetic C-scan generated using gprMax and the resulting SAR image for each transmitter-receiver pair. Notice that the range of the x-y coordinates changes for each transmitter-receiver pair. The isosurfaces are taken at a value of 0.7 (-3 dB). The final multistatic image is shown in Fig. 14. The isosurface is properly positioned at the center of the domain in the x-y plane (see Fig. 14 top-left). Furthermore, the top surface of the plate is correctly located at a depth of 0.1 m. However, the plate edges are not well recovered in the imaging process.

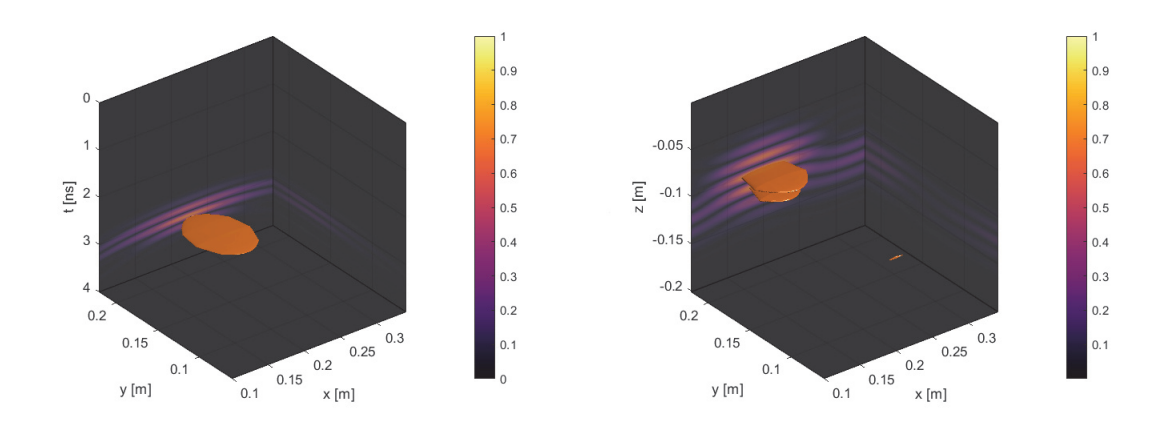


Figure 11. Plate S11 C-scan (left) and resulting 3D SAR image (right) isosurfaces at a value v = 0.7 (-3 dB).

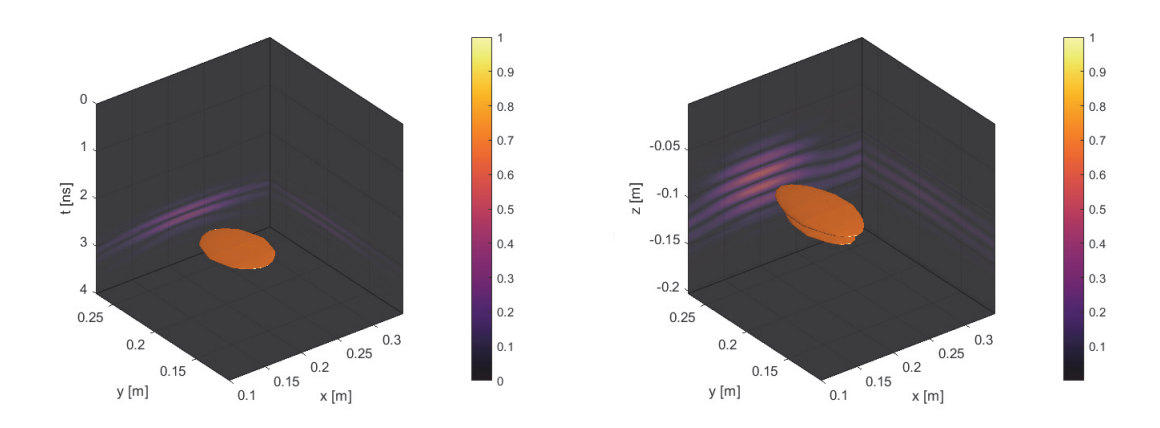


Figure 12. Plate S12 C-scan (left) and resulting 3D SAR image (right) isosurfaces at a value v = 0.7 (-3 dB).

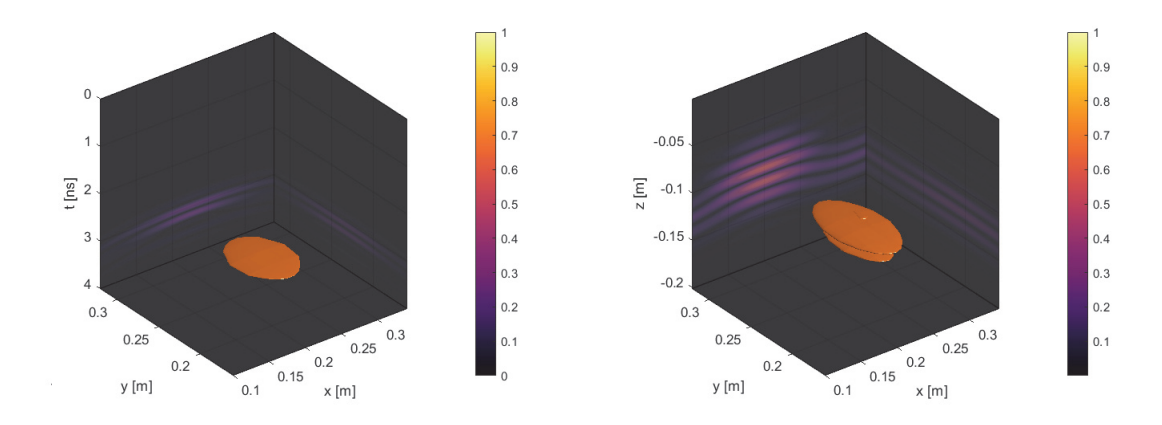


Figure 13. Plate S13 C-scan (left) and resulting 3D SAR image (right) isosurfaces at a value v=0.7 (-3 dB).

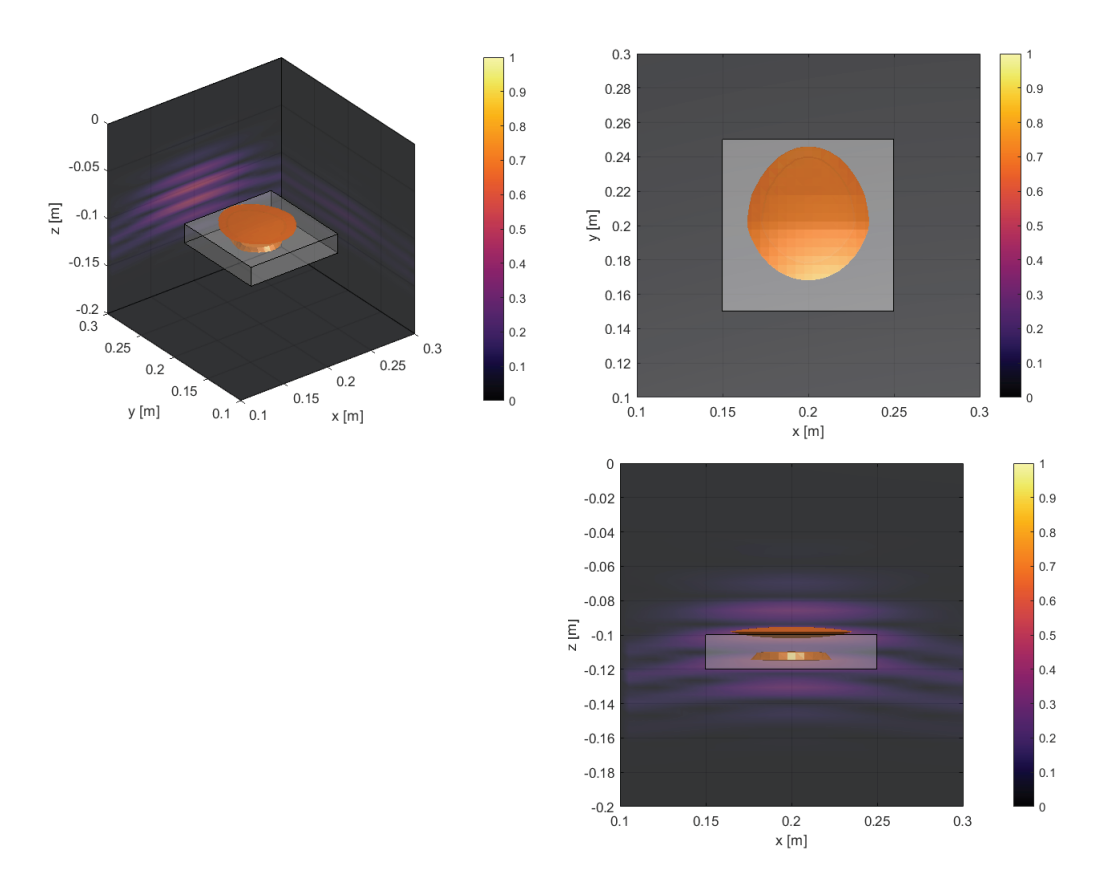


Figure 14. Final plate 3D multistatic image isosurface at v = 0.7 (-3dB) overlayed on 3D plate model.

4. CONCLUSIONS

In this paper, a SAR imaging algorithm for multistatic ground and air-coupled GPR was introduced. The algorithm provides an efficient way of fusing radar data from multiple antennas at the correct spatial position. In contrast to previously presented multistatic SAR imaging algorithms for layered media, the algorithm presented here does not rely on the assumption of a plane wavefront.

Furthermore, the method can be readily extended to any multi-layered media. Even if generating the reference signal used to determine Ψ_0 is slow, it may be performed offline only once and later used on multiple similar scenarios. For instance, in TWR, a single offline synthetic dataset may be generated for a small survey area, but used for any wall inspected as long as the the wall thickness, composition, and radar relative position to the wall is preserved.

A rigorous mathematical development is called for to address important parameters of SAR imaging. For instance, here a mapping on the time domain is used to adjust for the distortion caused by the variation in the wave speed, and interpolation in the frequency domain was not performed. Not performing interpolation may degrade the final image, and a comparison between the two approaches will be addressed in future work. An alternative to the mathematical derivation is to propose a model for the SAR spatial frequency mapping and determine the model parameters by using a set of reference known images.

In stripmap mode of satellite imaging the beamwidth of the antenna is small such that interpolation in the frequency domain may not required.²³ This same approximation is used here, but is not as well satisfied as in satellite imagery as the antenna is closer to the ground. However, the positive results presented support the use of this approximation. Furthermore, the final domain image must be discretized with enough points to have element size with at least half-wavelength of the most relevant frequency contributions to avoid aliasing when adding each transmitter-pair image.

Also, following the tradition of SAR imaging literature, amplitude terms are often ignored in the algorithm development. However, Li et al. shows that the SAR imaging algorithm can be derived from the inverse problem originating from Maxwell's equation of electromagnetism by using the Born approximation and other assumptions.¹⁷ In that development, the authors show that an amplitude term that emerges in the mathematical development, not due to the wavefront spread, is actually important for balanced image formation. For future work, this amplitude term may be investigated for better image focusing.

ACKNOWLEDGMENTS

This work is supported by the NSF Grants No. 1647095 and No. 1640687, the UVM SparkVT Fund and VT EPSCoR.

REFERENCES

- [1] Daniels, J. D., [Ground Penetrating Radar], The Institution of Electrical Engineers, London, UK, 2 ed. (2004).
- [2] Jol, H. M., [Ground penetrating radar: theory and applications], Elsevier Science, Amsterdam, Netherlands, 1 ed. (2009).
- [3] Fan, T., Xia, T., and Cheng, L., "Antenna performance under geo-property variations for real-time underground tomography," in [2016 IEEE International Geoscience and Remote Sensing Symposium (IGARSS)], 7426–7429, IEEE (2016).
- [4] Huston, D., Xia, T., Zhang, Y., Fan, T., Orfeo, D., and Razinger, J., "Urban underground infrastructure mapping and assessment," *Proc. of International Workshop on Structural Health Monitoring (IWSHM)* (2017).
- [5] Alani, A. M., Aboutalebi, M., and Kilic, G., "Applications of ground penetrating radar (GPR) in bridge deck monitoring and assessment," *Journal of Applied Geophysics* 97, 45–54 (2013).
- [6] Wang, Z. W., Zhou, M., Slabaugh, G. G., Zhai, J., and Fang, T., "Automatic Detection of Bridge Deck Condition from Ground Penetrating Radar Images," *IEEE Transactions on Automation Science & Engi*neering 8(3), 633–640 (2011).
- [7] Zhang, Y., Orfeo, D., Burns, D., Miller, J., Huston, D., and Xia, T., "Buried nonmetallic object detection using bistatic ground penetrating radar with variable antenna elevation angle and height," in [Nondestructive Characterization and Monitoring of Advanced Materials, Aerospace, and Civil Infrastructure 2017], 10169, 1016908, International Society for Optics and Photonics (2017).
- [8] Feng, X. and Sato, M., "Pre-stack migration applied to GPR for landmine detection," *Inverse Problems* **20**(6) (2004).
- [9] Halman, J. I., Shubert, K. A., and Ruck, G. T., "SAR processing of ground-penetrating radar data for buried UXO detection: results from a surface-based system," *IEEE Transactions on Antennas and Propa*gation 46(7), 1023–1027 (1998).
- [10] Ye, Q., Jiao, L., Liu, C., Cao, X., Huston, D., and Xia, T., "Extracting and identifying concrete structural defects in gpr images," in [Nondestructive Characterization and Monitoring of Advanced Materials, Aerospace, Civil Infrastructure, and Transportation XII], 10599, 1059919, International Society for Optics and Photonics (2018).
- [11] Zhang, Y., Venkatachalam, A. S., Huston, D., and Xia, T., "Advanced signal processing method for ground penetrating radar feature detection and enhancement," in [Nondestructive Characterization for Composite Materials, Aerospace Engineering, Civil Infrastructure, and Homeland Security 2014], 9063, 906318, International Society for Optics and Photonics (2014).
- [12] Zhang, Y. and Xia, T., "In-wall clutter suppression based on low-rank and sparse representation for through-the-wall radar," *IEEE Geoscience and Remote Sensing Letters* **13**(5), 671–675 (2016).
- [13] Zhang, Y., Candra, P., Wang, G., and Xia, T., "2-d entropy and short-time fourier transform to leverage gpr data analysis efficiency," *IEEE Transactions on Instrumentation and Measurement* **64**(1), 103–111 (2015).
- [14] Demirci, S., Yigit, E., Eskidemir, I. H., and Ozdemir, C., "Ground penetrating radar imaging of water leaks from buried pipes based on back-projection method," *NDT and E International* 47, 35–42 (2012).

- [15] Zhang, Y., Venkatachalam, A. S., and Xia, T., "Ground-penetrating radar railroad ballast inspection with an unsupervised algorithm to boost the region of interest detection efficiency," *Journal of Applied Remote Sensing* 9(1), 095058 (2015).
- [16] Cornick, M., Koechling, J., Stanley, B., and Zhang, B., "Localizing ground penetrating radar: A step toward robust autonomous ground vehicle localization," *Journal of Field Robotics* **33**(1), 82–102.
- [17] Li, L., Zhang, W., and Li, F., "Derivation and discussion of the SAR migration algorithm within inverse scattering problem: Theoretical analysis," *IEEE Transactions on Geoscience and Remote Sensing* **48**(1), 415–422 (2010).
- [18] Devaney, A. J., [Mathematical foundations of imaging, tomography and wavefield inversion], Cambridge University Press, New York, 1 ed. (2012).
- [19] Born, M. and Wolf, E., [Principles of Optics], Pergamon Press, Elmsford, NY, 6 ed. (1968).
- [20] Pereira, M., Zhang, Y., Orfeo, D., Burns, D., Huston, D., and Xia, T., "3d tomography for multistatic gpr subsurface sensing," in [Radar Sensor Technology XXII], 10633, 1063302, International Society for Optics and Photonics (2018).
- [21] Pereira, M., Zhang, Y., Orfeo, D., Burns, D., Huston, D., and Xia, T., "3D Tomographic Image Reconstruction for Multistatic Ground Penetrating Radar,," accepted by IEEE Radar Conference (RadarCon) (2019).
- [22] Gilmore, C., Jeffrey, I., and Lovetri, J., "Derivation and comparison of SAR and frequency-wavenumber migration within a common inverse scalar wave problem formulation," *IEEE Transactions on Geoscience and Remote Sensing* **44**(6), 1454–1460 (2006).
- [23] Soumekh, M., [Synthetic Aperture Radar Signal Processing with MATLAB Algorithms], John Wiley & Sons, New York, NY, 1 ed. (1999).
- [24] Curlander, J. C. and McDonough, R. N., [Synthetic Aperture Radar Systems and Signal Processing], John Wiley & Sons, New York, NY, 1 ed. (1991).
- [25] Abbasi, M., Shayei, A., Shabany, M., and Kavehvash, Z., "Fast Fourier-Based Implementation of Synthetic Aperture Radar Algorithm for Multistatic Imaging System," *IEEE Transactions on Instrumentation and Measurement PP*, 1–11 (2018).
- [26] Zhang, W., Hoorfar, A., and Thajudeen, C., "Building layout and interior target imaging with SAR using an efficient beamformer," *IEEE Antennas and Propagation Society, AP-S International Symposium (Digest)* (1), 2087–2090 (2011).
- [27] Fallahpour, M., Case, J. T., Ghasr, M. T., and Zoughi, R., "Piecewise and wiener filter-based sar techniques for monostatic microwave imaging of layered structures," *IEEE Transactions on Antennas and Propagation* **62**(1), 282–294 (2014).
- [28] Yarman, C. E., Yazici, B., and Cheney, M., "Bistatic synthetic aperture inversion for arbitrary flight trajectories," Algorithms for Synthetic Aperture Radar Imagery XIV 6568(1), 656807 (2007).
- [29] Nolan, C. J. and Cheney, M., "Synthetic aperture inversion," Inverse Problems 18(1), 221–235 (2002).
- [30] Krishnan, V., Swoboda, J., Yarman, C. E., and Yazici, B., "Multistatic synthetic aperture radar image formation," *IEEE Transactions on Image Processing* **19**(5), 1290–1306 (2010).
- [31] Zhang, W. and Hoorfar, A., "Three-dimensional synthetic aperture radar imaging through multilayered walls," *IEEE Transactions on Antennas and Propagation* **62**(1), 459–462 (2014).
- [32] Soumekh, M., "Bistatic synthetic aperture radar inversion with application in dynamic object imaging," *IEEE transactions on signal processing* **39**(9), 2044–2055 (1991).
- [33] Papoulis, A., [Systems and Transforms with Applications in Optics], John Wiley & Sons, New York, NY, 1 ed. (1968).
- [34] Warren, C., Giannopoulos, A., and Giannakis, I., "gprMax: Open source software to simulate electromagnetic wave propagation for Ground Penetrating Radar," Computer Physics Communication 209, 163–170 (2016).